Journal of Magnetism and Magnetic Materials 514 (2020) 167102

Contents lists available at ScienceDirect

Journal of Magnetism and Magnetic Materials

journal homepage: www.elsevier.com/locate/jmmm

Research articles

Local-field effect on the hybrid ferromagnetic-diamagnetic response of opals with Ni nanoparticles

C.E. Ávila-Crisóstomo[a,*], Umapada Pal[a], F. Pérez-Rodríguez[a], M.G. Shelyapina[b], A.A. Shmyreva[c,b]

[a] Instituto de Física, Benemérita Universidad Autónoma de Puebla, Apdo.Postal J-48, Puebla, Pue 72570, Mexico
[b] Saint-Petersburg State University, 7/9 Universitetskaya nab, St.Petersburg 199034, Russia
[c] Department of Low Temperature Physics, Faculty of Mathematics and Physics, Charles University, Prague, Czech Republic

ARTICLE INFO

Keywords:
Nanocomposite
Opal
Nanoparticles
Ferromagnetism

ABSTRACT

The magnetic properties of artificial opals infiltrated with nickel nanoparticles are studied both experimentally and theoretically. The response of the composite has a dominating ferromagnetic behavior at low magnitude fields (below the saturation region), then it is followed by a dominating diamagnetic one as the intensity of the external applied field is increased. These characteristics are not observed in most cases due to the low magnetic response of the elements involved. Diamagnetism in the artificially synthesized opals was observed, having a negative volume magnetic susceptibility of the order of 10^{-5}. Also theoretical calculations were performed on the basis of the Landau-Lifshitz-Gilbert (LLG) equation, taking into account the diamagnetic response of the host material. Results obtained show the importance of the local magnetic field on the ferromagnetic nanoparticles, as well as the importance of the nature of the magnetic response of SiO_2 spheres, which aligns in the opposite direction of the external applied field.

1. Introduction

Composites are well known for their interesting and novel physical and chemical properties. The study of this kind of materials, either for determining their fundamental properties or for the development of novel applications, is of considerable interest. Soft Magnetic Composites (SMCs) are well known for their improved low frequency properties and suitable alternative to laminated materials, because of their isotropic response and shaping possibilities for 3D-design applications [1]. Magnetic nanocomposites have been used for cleanup of pesticides [2], hyperthermia and drug release for cancer treatment [3] and catalysis [4], just to mention some applications.

Opal matrices are widely used as hosts for several types of materials. Their periodically arranged void structure is used to impose long range ordering to the infiltrated material. Semiconductors [5–7] and metallic nanoparticles [8–10] are some of the preferred materials to introduce into the opal matrix in order to tailor some of their physical properties. Magnetic nanoparticles are also incorporated in the artificial opal mainly to modify the optical properties (see for example [11–16]). In this work, we experimentally and theoretically study the magnetic behavior of such nanocomposites in the quasistatic case. Similar systems have been studied previously lacking the proper theoretical description when the magnetic response of the nanocomposite is dominated by the host matrix, for example, Ni clusters inside a carbon matrix [17] or Co nanoparticles in a PMMA matrix [18].

2. Experimental section

2.1. Artificial opals synthesis

Colloidal SiO_2 spheres were synthesized by the Stöber [19] process by which it is possible to control the size of the obtained spheres as well as to obtain monodispersity. Reagents used in this procedure were tetraethylorthosilicate (TEOS Sigma–Aldrich 98%), absolute ethanol (J. T. Baker 99.95%) and ammonium hydroxide (NH_4OH J. T. Baker 29.6%) in concentrations of 0.014 M, 2.15 M and 0.46 M respectively and 2.89 M of deionized water according to [20], where ethanol, water and ammonium hydroxide concentrations are constant and only by varying TEOS concentration the colloidal spheres diameter is controlled. Reagents were mixed at room temperature and kept stirring for 2 h. SiO_2 spheres were separated by centrifugation and washed 3 times with deionized water and 3 more times with absolute ethanol. Then a selection method of spheres was employed to get a better sedimentation according to [21]. The fcc self-assembly of SiO_2 colloidal spheres with [111] as the growing direction has been extensively studied elsewere [22–24]; thermodynamic reasons for the growth in a fcc structure over

* Corresponding author.
E-mail address: cavila@ifuap.buap.mx (C.E. Ávila-Crisóstomo).

https://doi.org/10.1016/j.jmmm.2020.167102
Received 3 December 2019; Received in revised form 27 May 2020; Accepted 2 June 2020
Available online 20 June 2020
0304-8853/ © 2020 Elsevier B.V. All rights reserved.

a hexagonal one are presented in [25]. After sedimentation, annealing of the crystallized structures was carried out at 800°C for three hours, which improves mechanical properties and modifies optical properties of the artificial opal [6].

2.2. Ni nanoparticles synthesis

The common methods to obtain Ni nanoparticles rely on chemical reduction of Ni precursor salts in different type of solvents as well as with different kind of reducing agents [26], besides some others such as electrochemical deposition [27] and microemulsion technique [28]. In this work, Ni nanoparticles were obtained by means of the reduction of nickel acetate ($Ni(CH_3COO)_2{\cdot}4H_2O$ Sigma Aldrich 99%) with hydrazine (N_2H_4 Sigma Aldrich 98%) in ethylene glycol ($HOCH_2–CH_2OH$ Alfa-Aesar 99%). The synthesis consisted in the dissolution of 0.1381 g of nickel acetate in 18 ml of ethylene glycol during one hour at 60 °C under magnetic stirring. In a similar procedure, 75 mg of hydrazine were dissolved in 1.427 ml of ethylene glycol and added to the Ni precursor solution at 83 °C. Then a solution of 2.7 mg of sodium hydroxide (NaOH) in 4.5 ml of the same solvent was added to the whole mixture. After one hour of magnetic stirring in a capped bottle, the solution turned black, indicating that the reduction of Ni^{2+} to Ni^0 took place. The general reduction reaction can be expressed as follows:

$$2Ni^{2+} + N_2H_4 + 4OH \rightarrow 2Ni^0 + N_2 + 4H_2O.$$

2.3. Opals containing Ni nanoparticles

Different methods regarding the opal matrix void infiltration are described elsewhere [9,5,29]. In order to obtain the SiO_2 opal with infiltrated Ni nanoparticles a previously synthesized opal was immersed in a colloidal solution ($5{\times}10^{-4}$ M) of Ni nanoparticles in hexane following a procedure similar to the one reported in [30].

2.4. Characterization

Scanning electron microscopy (SEM) images were obtained with a Jeol JSM-7800F microscope equipped with an Oxford X-Max 50 microprobe for the energy dispersive X-ray spectroscopy analysis (EDS). ^{61}Ni NMR measurements were carried out using aTecmaq RedStone NMR spectrometer under zero external magnetic field at room temperature. For NMR spectra recording, the standard spin-echo pulse sequence (p1-τ-p2) was used. This is a very sensitive method of studying structural and magnetic properties of magnetic materials [31,32] which resolves individual spectral lines of nuclei in a different local environment. The ^{61}Ni NMR data were collected from the powdered sample placed inside a copper coil of a tuned probe. To obtain NMR spectra the amplitude of the spin-echo signal as a function of the pulse frequency was measured, and spectra were plotted point by point with increments of about 0.25 MHz. The lengths of both p1 and p2 pulses were equal to 0.3 μs, with the delay between pulses $\tau = 35$ μs. During spectrum recording a fixed rf field pulse durations and amplitudes were used. Magnetization curves of the samples were recorded in a Quantum Design PPMS Dyna Cool-9 physical properties measurement system (PPMS) with a vibrating sample magnetometer (VSM) module. For each sample 14 constant temperature loops were obtained with an applied magnetic field normal to the film surface, i.e. along the growth direction [111] of the pristine opal and the composites. Ni nanoparticles were measured as powder.

3. Experimental results

3.1. Structure and composition

In Fig. 1(a), a typical SEM image of the surface of the crystallized opal structure is shown. The micrograph depicts a hexagonal surface

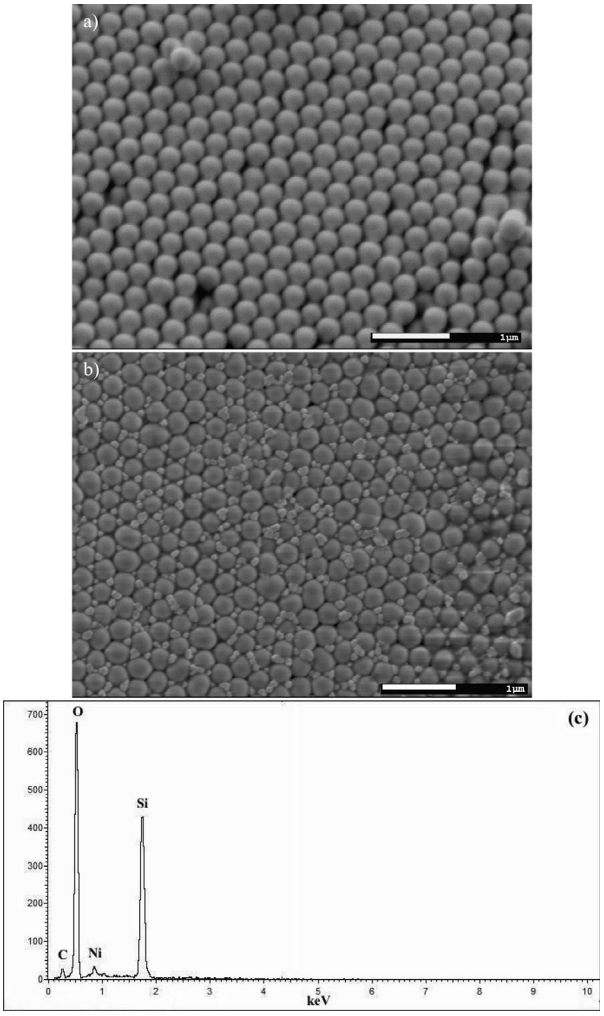

Fig. 1. SEM micrograph of the crystallized SiO_2 opal structure before (a) and after infiltration of the Ni nanoparticles (b) and EDS analysis of the infiltrated opal (c).

typical of the (111) plane in a fcc structure. In order to obtain the size distribution of the SiO_2 colloidal spheres conforming the opal structure the diameters of 532 spheres were measured from the SEM micrographs by means of the *ImageJ* software, which is of public domain. According to the histogram obtained from such measurements a gaussian curve was fitted. The average diameter of the spheres is 304 nm and standard deviation is of 13.93 nm, which implies a 4.5% variation from the average value. Fig. 1(b) corresponds to the artificial opal infiltrated with Ni nanoparticles. Clusters of Ni nanoparticles are clearly seen on the voids of the periodic structure of colloidal spheres. The lack of clusters covering greater parts of the sample surface suggests that the metallic nanoparticles are spread only in the interstitial voids. Confirmation of the elements that constitute the sample is presented in Fig. 1(c).

In Fig. 2(a) and (b) the Ni nanoparticles synthesized with the described method in the experimental section are shown. Fig. 2(a) shows particles that appear to be in the 100 nm range but in Fig. 2(b) it can be appreciated that they are clusters that consist of smaller particles joined by magnetic interactions. For this reason the determination of the average size is not properly obtained from SEM images.

Nowadays nuclear magnetic resonance (NMR) is a tool widely used in chemistry or biology [33]. However, it can be also successfully applied to probe ferromagnetic nanosized systems, providing information on the structure, interface morphology and magnetic properties of magnetic nanomaterials [34–36]. Because in magnetically ordered

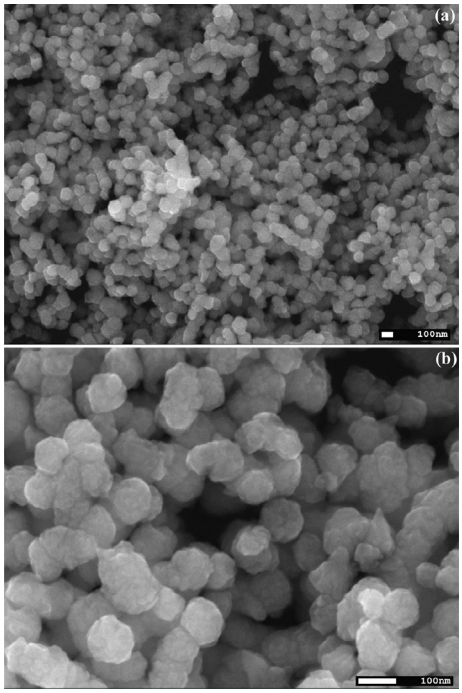

Fig. 2. SEM micrograph of the Ni nanoparticles.

materials due to hyperfine interactions there are large and fairly homogeneous magnetic fields on the nuclei of paramagnetic ions, NMR can be observed without an external magnetic field [33]. This method is often called zero-field NMR. The main advantage of NMR compared to more traditional methods to study sample morphology (such as TEM, for example) is that, on the one hand, it does not require any specific sample preparation, and on the other hand, it provides analysis on the larger scale (several mg of the sample) without statistical accumulation of the local data. The room temperature zero-field ^{61}Ni NMR spectrum of nickel nanoparticles recorded at optimal radio frequency (rf) field amplitude (14 dB) is shown in 3. The spectrum has a rather complex shape with more pronounced two inhomogeneously broadened peaks at 26.13 and 26.54 MHz (corresponding to hyperfine field B_{hf} = 6.87 and 6.98 T using the ^{61}Ni gyromagnetic ratio 3.8046 MHz T^{-1}), respectively, with integral intensity ratio of about 2:1. Such a double humped shape for Ni nanoparticles was earlier reported in [37]. Based on a complimentary NMR spectroscopy and spin–spin relaxation study, the authors attributed the lower and higher frequencies to the surface and interior part of a nanoparticle. According to studies reported in [38], at room temperature the ^{61}Ni NMR frequency signal for the bulk fcc Ni represents a relatively narrow line at 26.1 MHz. At low temperature (below 4.2 K) the ^{61}Ni signal for metallic Ni was reported at about 29 MHz [37,39]. Thereby, the two lines represented in Fig. 3 can be attributed to the core with fcc structure (higher frequency) and surface (lower frequency) of Ni particles in size < 100 Å. However, the more complex line shape, e.g. the presence of an additional shoulder at 25.24 MHz, refers to an inhomogeneous distribution of the particle size, that is in agreement with SEM image shown in Fig. 1(b).

3.2. Magnetic response

In Fig. 4 the magnetization curves of the Ni nanoparticles is shown. The Ni nanoparticles revealed common ferromagnetic response in the whole temperature range (2–300 K). The hysteresis curves show an increment in the magnitude of the coercive field (H_c) as well as the saturation magnetization (M_s) when the temperature is decreased, typical features of a ferromagnetic material.

In Fig. 5 the magnetic behavior of the nanocomposite is shown. The

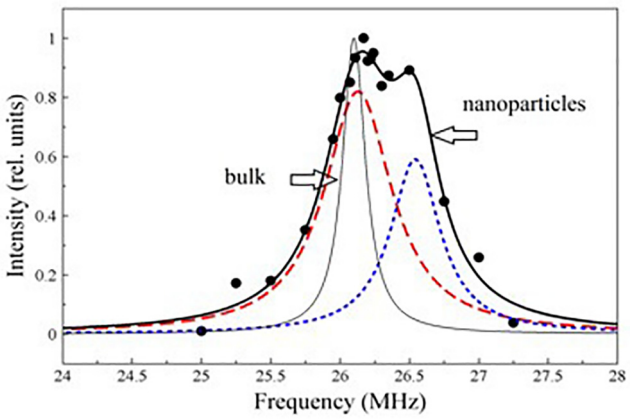

Fig. 3. ^{61}Ni NMR spectrum of Ni nanoparticles at room temperature. The spectrum from bulk Ni reported in [37] is also shown for reference. The dashed lines show the decomposition of the experimental spectrum on two Voigt lines from core and surface Ni atoms.

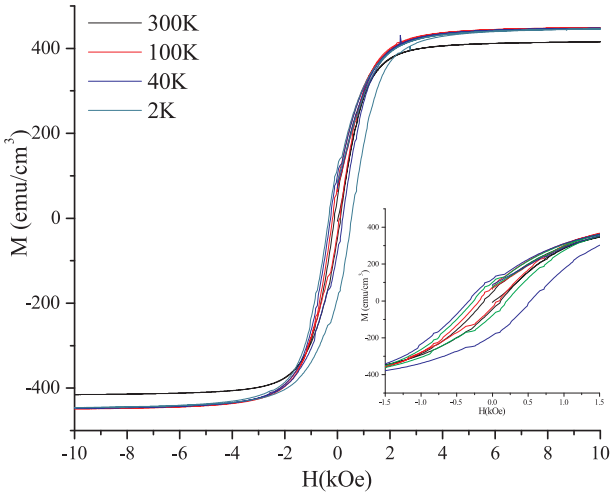

Fig. 4. Magnetization curves of the as synthesized Ni nanoparticles.

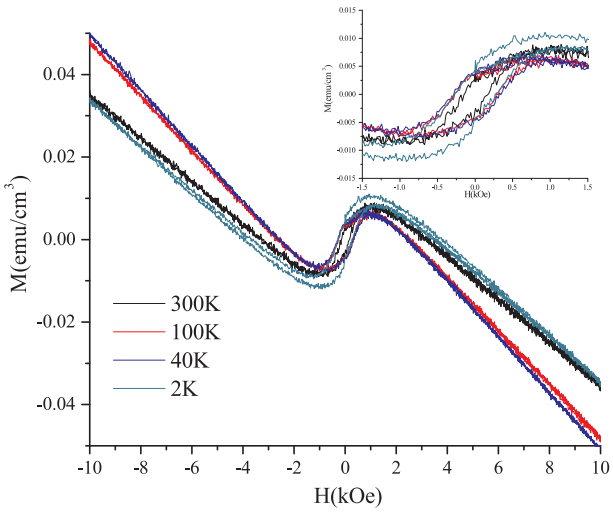

Fig. 5. Magnetization curves of the artificial opal matrix infiltrated with Ni nanoparticles.

sample was weighted before VSM measurements were carried out (2.5 mg). Then, the volume is calculated with the density of the pristine opal (1.67 g cm^{-3}) according to [40]. The volume of the nickel

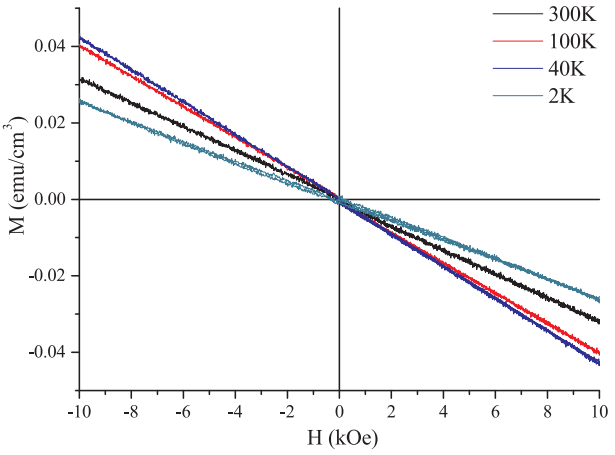

Fig. 6. Magnetization curves of the artificial opal.

nanoparticles is neglectable because they are allocated in the interstitial sites and their weight is, in relation with the ferromagnetic response of the nanocoposite in experimental measurements, estimated in 1.15 μg. We work with volume normalization in order to associate the magnetization curves with the magnetic susceptibility (χ). There is a region where the response of the ferromagnetic elements is the main contribution to the total magnetization of the sample, that is until saturation is reached, after that the diamagnetic elements response takes the dominating role due to their dependence on the strength of the external applied field.

The hybrid diamagnetic–ferromagnetic behavior was an unexpected result, therefore, to corroborate it, a magnetization curve of the pristine opal was obtained, shown in Fig. 6. Here a negative magnetic susceptibility increases in magnitude with the decrease of temperature until a maximum is reached at 40 K. At temperatures lower than 40 K the magnetic susceptibility decreases in magnitude. This measurement provided insight about the nature of the diamagnetic section in Fig. 5.

It should be noted that the magnitude of magnetic susceptibility of the pristine opal is smaller than that of the composite, i. e. the slope of the linear region of the composite for the whole temperature range as can be seen in Fig. 7. Another feature of the composite is the existence of four different values of the external magnetic field where the same magnetization is measured (in the region of $|M| \leqslant |M_s|$); this being in contrast with the common behavior of a hysteresis curve for a

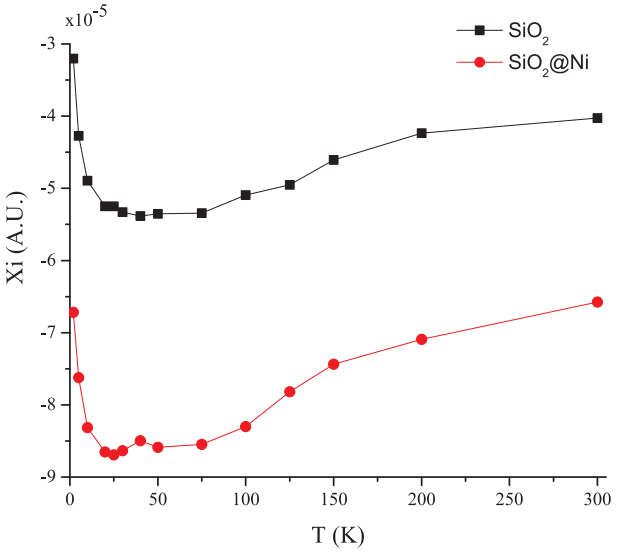

Fig. 7. Comparison between the artificial opal and the nanocomposite magnetic susceptibilities.

ferromagnetic material as the one shown in Fig. 4 where only two values of the external applied field cause the same magnetization in the material.

4. Theoretical model

4.1. Magnetic local field

In a previous study of a similar system, namely SiO_2 artificial opals infiltrated with Fe nanoparticles, the role of the magnetic interaction between different sites of the interstitial lattice was modeled [41]. One of the main conclusions of that study was the almost irrelevant influence of the magnetic dipolar interactions between different interstitial sites on the total magnetic response of the system. This led us to develop another model which represents better the actual mechanisms that are taking place in this kind of nanocomposites. It is important to state the difference between the local magnetic field ($\vec{H}_{\mathrm{loc}}$) that acts on each of the magnetic dipoles which constitute the sample and the macroscopic one ($\vec{H}$), related with experimental measurements. The latter because of the crucial role of the magnetic local field in the Landau–Lifshitz–Gilbert equation (LLG). In such systems the local magnetic field can be expressed as [42]:

$$\vec{H}_{\mathrm{loc}} = \vec{H}_0 - N\vec{M} + \frac{1}{3}\vec{M} + \vec{H}_{\mathrm{dip}} + \vec{H}_{\mathrm{a}}, \tag{1}$$

where the right terms of the equation correspond to the external, demagnetization, Lorentz, dipolar and magnetic anisotropy fields respectively. It is commonly used to get rid of the dipole–dipole interactions, however, in this case it is an important contribution to the total magnetic response of the sample. Regarding the terms involving the total magnetization of the sample, namely the demagnetization and the Lorentz fields, we can dispose of them with no relevant consecuences due to the magnitude of the nanocomposites magnetization. The latter is justified because the total magnetization of the artificial opals infiltrated with Ni nanoparticles is in the order of 10^{-2} emu cm^{-3} (Fig. 4), whereas the change in the external applied magnetic field in each step of the measurement is of 20 Oe (251 emu cm^{-3}). These changes leave the following expression for the local magnetic field:

$$\vec{H}_{\mathrm{loc}} = \vec{H}_0 + \vec{H}_{\mathrm{dip}} + \vec{H}_{\mathrm{a}}. \tag{2}$$

4.2. Magnetic clusters surrounded by diamagnetic spheres

The common approach when dealing with composites is to use either the Maxwell Garnett or Bruggeman theory to describe the total response of the system to an applied external field [43–45], nonetheless, this is only valid for systems whose response to an external field is linear. In this case, the spatial distribution of the different components of the sample is well known and it can be used to include the magnetic response of each one explicitly; in addition, the magnetic response of the artificial opal is linear and because it is comprised of SiO_2 colloidal spheres, an explicit mathematical form for its magnetic response can be applied. So, the magnetic dipolar field acting on the i-th ferromagnetic moment has the following form:

$$\vec{H}_{\mathrm{dip},i} = -\frac{1}{4\pi}\sum_{j=1,j\neq i}^{N}\left(\frac{\vec{\mu}_j}{r_{ij}^3} - 3\frac{(\vec{\mu}_j\cdot\vec{r}_{ji})\vec{r}_{ji}}{r_{ji}^5}\right) - \frac{1}{4\pi}\sum_{k=1}^{D}\left(\frac{\vec{\nu}_k}{r_{ik}^3} - 3\frac{(\vec{\nu}_k\cdot\vec{r}_{ki})\vec{r}_{ki}}{r_{ki}^5}\right), \tag{3}$$

where N is the number of ferromagnetic moments in the cluster, D the total number of diamagnetic ones, $\vec{\mu}_j$ is one of the ferromagnetic moments and $\vec{\nu}_j$ is the magnetic moment of a diamagnetic sphere. It is important to state that only the influence of the diamagnetic moments on the ferromagnetic ones is considered and not vice versa. The reason is the linear response to the external applied field from the diamagnetic

moments and the low intensity of the magnetic field due to ferromagnetic clusters compared with the external applied field. An estimation of the intensity of the magnetic field from a ferromagnetic cluster, given the values used for theoretical calculations and considering the conditions for a maximum intensity of H_{dip}, is of 6.84 A m^{-1} (0.086 Oe). The diamagnetic response of the artificial opal is described using the magnetization of a diamagnetic sphere as follows [46]:

$$\vec{M}_{sph} = 3\frac{\mu - 1}{\mu + 2}\vec{H}, \tag{4}$$

where μ stands for the magnetic permeabilty of the sphere and $\vec{H}$ is the macroscopic magnetic field. Reformulating in terms of the magnetic susceptibility and the magnetic moment:

$$\vec{\nu}_{sph} = 3V_{sph}\frac{\chi_{sph}}{\chi_{sph} + 3}\vec{H}_0, \tag{5}$$

where V_{sph} is the volume of the sphere. The macroscopic field is, for the reasons stated in the previous section, the external applied field. Relating the magnetic susceptibility of each sphere with the one obtained from experimental measurements of the opal magnetization, taking into account the geometrical aspects of the structure, results in the following expression:

$$\chi_{sph} = \frac{3\sqrt{2}}{\pi}\chi_{op}, \tag{6}$$

where χ_{op} is the magnetic susceptibility of the artificial opal (Fig. 5). Eq. 6 relates the experimental magnetic susceptibility obtained from experimental measurements on the pristine artificial opal and the magnetic susceptibility of one sphere, needed to calculate is magnetic moment by means of Eq. 5.

Therefore, the magnetization of the system is expressed as:

$$M = \frac{1}{V_c}\left(\sum_{i=1}^{N}\vec{\mu}_i\cdot\hat{h} + \sum_{j=1}^{D}\vec{\nu}_j\cdot\hat{h}\right), \tag{7}$$

where $\hat{h}$ is a unit vector in the direction of the external applied field and V_c is the volume of the unit cell (Fig. 8).

Now we can express the LLG eq. for the i-th ferromagnetic element as follows [47–49]:

$$\frac{d\vec{M}_i}{dt} = -\gamma\vec{M}_i \times \vec{H}_{eff,i} - \alpha\frac{\gamma}{M_s}\vec{M}_i \times (\vec{M}_i \times \vec{H}_{eff,i}), \tag{8}$$

where $\vec{M}_i$ is the magnetization of the i-th magnetic moment, γ is the gyromagnetic ratio, α is a dimensionless constant and $\vec{H}_{eff,i}$ is the effective magnetic field acting on the i-th element, which has the form:

$$\vec{H}_{eff,i} = \vec{H}_0 + \frac{H_a}{|\vec{M}_i|}(\vec{M}_i\cdot\vec{n}_i)\vec{n}_i + \vec{H}_{dip,i}, \tag{9}$$

with $\vec{H}_0$ as the external magnetic field, the second term is the magnetic anisotropy field, inherent to every ferromagnetic element

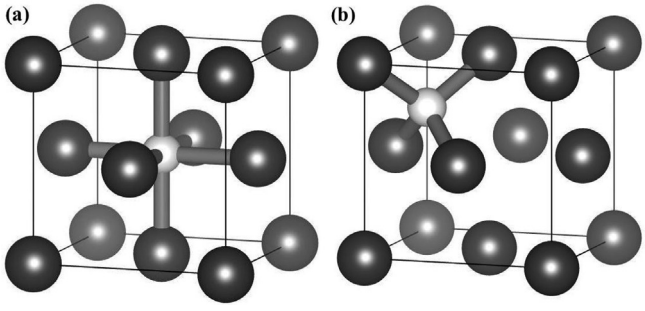

Fig. 8. Fcc structure showing the possible interstitial occupation for the magnetic clusters: octahedral sites (a) and tetrahedral sites (b).

($H_a = 2K_a/\mu_0 M_s$, K_a is the anisotropy constant, μ_0 the vacuum magnetic permeability, M_s the saturation magnetization and $\vec{n}$ is a unit vector corresponding to the anisotropy axis) and the last term corresponds to dipolar interactions previously described in Eq. 3.

5. Numerical results

Theoretical curves were obtained by numerically solving the LLG equations employing a fortran code based on the Shampine's algorithm [50] for integrating ordinary differential equations. In the quasi-static case, for each change in magnetic field magnitude, the system is relaxed and only then another point of the curve is obtained. The program labels each ferromagnetic moment in the cluster and assigns a random unit vector for the magnetic anisotropy inherent to each one, in addition, positions are assigned randomly within a cube whose volume is previously fixed. In every calculation, a magnetic cluster stands in the center of coordinates surrounded by diamagnetic spheres as depicted in Fig. 8. To model the infiltrated opal 12 clusters were considered, each formed by 22 ferromagnetic moments; 4 of the clusters representing octahedral sites and 8 of them tetrahedral sites. The total number of diamagnetic spheres, each associated to a diamagnetic moment, is irrelevant to the magnetization according to ecs. 5, 6 and the total volume of the system. Each cluster is surrounded by the proper number of diamagnetic spheres (4 for the tetrahedral and 6 for the octahedral sites). Results presented are the average of clusters equivalent to 10 unit cells, each made of 8 in tetrahedral sites, 4 in octahedral and 4 diamagnetic spheres, but the latter does not imply that all of the clusters are in the same unit cell as they only interact with its surrounding diamagnetic spheres. The particular parameters used in our calculation for nickel nanoparticles are the gyromagnetic ratio of nickel [51] $\gamma = 2.21 \times 10^5 (mA^{-1}s^{-1})$, a damping constant $\alpha = 0.066$ (which is generally less than 0.1 for iron, cobalt and nickel). Some of the parameters provided are $\mu = 3 \times 10^{-18}$ A m^2;$k_1 = 2.23 \times 10^4$ J m^{-3};$\chi_{op} = -8.49 \times 10^{-5}$;$r = 150$ nm; $V_T = 3.81 \times 10^{-17}$ m^3, which are the magnitude of the magnetic moment, magnetic anisotropy constant, magnetic susceptibility (in Fig. 7 SiO_2@Ni at 40 K), radius of the spheres and the total volume. μ and k_1 are fitted parameters; χ_{op} is an actual parameter of the nanocomposite previously mentioned, r is the actual radius of the synthesized SiO_2 spheres and V_T is the total volume of the system, calculated as $4\sqrt{2}Nr^3$; where N is the number of diamagnetic spheres, in this case 2000 (500 unit cells). Ferromagnetic moments are distributed randomly within a virtual cube of 30 nm by side but the magnitude of the magnetic moment used in calculations corresponds to a cluster which volume is equal to a sphere of 64 nm in diameter. The program generates three random unit vectors in cartesian coordinates for each position of a ferromagnetic moment and then multiplies it by the desired value provided from the user, in this case 30 nm, since this was the best fit to the experimental measurement. The size of the virtual cube is directly related with the intensity of the dipole–dipole magnetic interactions (Eq. 3) and its effect is observed in the "skewness" of the magnetization curve. Results are presented in Fig. 9(c). Parameters used to calculate the magnetization curve in Fig. 9(d) are $\alpha = 0.066$, $\chi = -8.6 \times 10^{-5}$ which are dimensionless and correspond to the damping constant and the magnetic susceptibility of the opal matrix; $\gamma = 2.21 \times 10^5$ Hz m A^{-1} is the gyromagnetic ratio for ferromagnetic moments corresponding to nickel nanoparticles; $\mu = 8.1 \times 10^{-20}$ A m^2 for each of the 22 ferromagnetic moments present in the unit cell (14 in octahedral sites and 8 in tetrahedral ones) but considering their occupancy in the unit cell (Fig. 8); $k_1 = 2.239 \times 10^4$ J m^{-3} and $V_c = 7.63 \times 10^{-20}$ m^3. All the previous parameters listed before are taken from the experimental magnetization curve presented in Fig. 9(a), except for the damping constant and the gyromagnetic ratio. The theoretical formalism for the calculation of the ferromagnetic dipole–dipole interactions in a periodic lattice, used for the calculation of Fig. 9(d) is described in [41]. The main idea is to calculate H_{dip} based on the periodic structure imposed on the infiltrated ferromagnetic

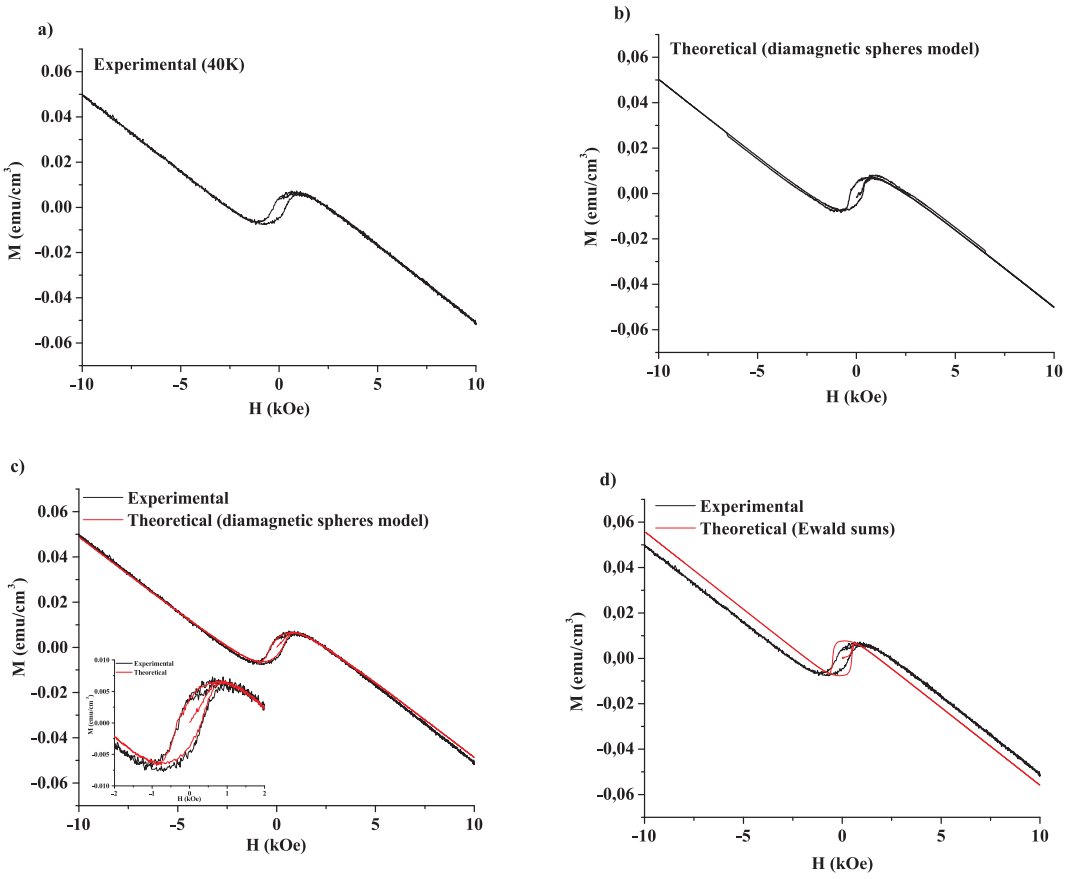

Fig. 9. Magnetization curves for the artificial opal infiltrated with nickel nanoparticles. Curves correspond to: experimental measurements at 40 K (a), theoretical curve (diamagnetic spheres model) (b), comparison between theoretical and experimental results (diamagnetic spheres model) (c) and comparison between theoretical and experimental results (Ewald summation model) [41].

nanoparticles, in this case nickel nanoparticles, and considering only one ferromagnetic moment per interstitial site as one can consider a bulk sample with an average magnetic moment. Also, the diamagnetic response is taken directly from the experimental magnetization curve in the parameter χ Fig. 9(a). This is in clear contrast with the approximation presented here, where we focus on the calculation of H_{dip} within each of the interstitial sites and take into account explicitly the diamagnetic moments of the silica spheres that surround each ferromagnetic cluster. Furthermore, the role of dipole–dipole interactions between clusters in different interstitial sites has no relevant effect on the magnetization curve for this system. The good fit between the calculated and experimental results is evident in Figs. 9(c) and 9(d). Another aspect to notice is the influence of the local dipolar field in the overall shape of the curve, being more accurate in relation with the experimental results. With "local magnetic field" we refer to the dipole–dipole interactions between ferromagnetic moments within a cluster in an interstitial site. This is in clear contrast with the curve calculated in Fig. 9(d) for the reasons previously mentioned. Moreover, there is no relation between the responses of the diamagnetic and ferromagnetic elements in the nanocomposite in the framework presented in [41], where we obtain most of the parameters used in calculations from the experimental curve. Thus, the consideration of the local dipolar field emulates the response of the nanocomposite to an external magnetic field congruently with the experimental measurements. Finally a rough estimation of the concentration of Ni nanoparticles in the opal can be carried out from two points of view, experimental measurements and theoretical calculations. The first one is concerned with the saturation magnetization (M_s) in both (Figs. 4 and 5) experimental measurements at 40 K. These values are 447.26 emu cm^{-3} and 6.73×10^{-3} emu cm^{-3} respectively, resulting in an estimated volume fraction of Ni nanoparticles in the opal matrix of 0.001%. Some assumptions must be taken into account to make the latter estimation; the value of the "saturation" magnetization of the infiltrated opal is taken just before the magnetization curve in Fig. 4 begins to have a linear behavior and the diamagnetic response of the nanocomposite is not taken into account. When the estimation is based on theoretical calculations the diamagnetic response of the system is emulated. There are 22 magnetic moments of 3×10^{-15} emu in each cluster per interstitial site, and calculations are based on 12 clusters in total (8 tetrahedral and 4 octahedral). This gives us 7.92×10^{-13} emu in the artificial opal. So, with M_s from Fig. 4 and the volume of the unit cell we estimate a volume fraction of 0.0046% in the nanocomposite. A posible explanation for such a low concentration of ferromagnetic material may be due to the size of the clusters, being close to the maximal volume available for a sphere in a tetrahedral site ($r_{max}\approx 34nm$), which prevents ferromagnetic nanoparticles from reaching deeper into the artificial opal.

6. Conclusions

The main objective of this work is to describe the possible mechanisms that take an active role in the magnetic response of the system. We showed that when we model the clusters in the interstitial sites of the artificial opal as an effective ferromagnetic moment (Fig. 9(d)), the resulting curve does not represent adequately the features observed in the experimental measurements, thus, dipole–dipole interactions between clusters in different interstitial sites has no relevance in these kind of systems. With "local field" we refer to the explicit calculation of dipole–dipole magnetic interactions that take part in a magnetic cluster, namely the expression in Eq. 3, which is able to properly describe the phenomenon (Fig. 9(c)). Therefore, the actual

concentration of ferromagnetic material can be inferred from theoretical calculations of the magnetization curve. This model can be extended to disordered nanocomposites by the calculation of random configurations of the constituents.

CRediT authorship contribution statement

C.E. Ávila-Crisóstomo: Conceptualization, Methodology, Software, Formal analysis, Writing - original draft. **U. Pal:** Resources, Writing - review & editing. **F. Pérez-Rodríguez:** Conceptualization, Methodology, Writing - review & editing, Supervision, Funding acquisition. **M.G. Shelyapina:** Resources, Writing - original draft, Writing - review & editing. **A.A. Shmyreva:** Investigation, Writing - review & editing.

Declaration of Competing Interest

The authors declare that they have no known competing financial interests or personal relationships that could have appeared to influence the work reported in this paper.

Acknowledgments

This work was partially supported by PRODEP, PFCE, and VIEP-BUAP. The NMR studies were carried out at the Centre for Magnetic Resonance of the Research Park of Saint Petersburg State University.

References

[1] L.O. Hultman, A.G. Jack, Soft magnetic composites-Materials and Applications, Electric Machines and Drives Conference, 2003. IEMDC'03. IEEE International, vol. 1, IEEE, 2003, pp. 516–522.
[2] L.C. Shen, C. Liu, J. Korringa, K.J. Dunn, Computation of conductivity and dielectric constant of periodic porous media, J. Appl. Phys. 67 (11) (1990) 7071–7081.
[3] S. Purushotham, R.V. Ramanujan, Thermoresponsive magnetic composite nanomaterials for multimodal cancer therapy, Acta Biomater. 6 (2010) 502–510.
[4] H. Lei, et al., The preparation and catalytically active characterization of papain immobilized on magnetic composite microspheres, Enzyme Microb. Technol. 35 (2004) 15–21.
[5] J. Zou, et al., Thermally tuning of the photonic band gap of SiO_2 colloid crystal infilled with ferroelectric $BaTiO_3$, Appl. Phys. Lett. 78 (5) (2001) 661–663.
[6] H. Míguez, et al., Face centered cubic photonic bandgap materials based on opal-semiconductor composites, J. Lightwave Technol. 17 (11) (1999) 1975–1981.
[7] V. N. Bogomolov, et al., Fabrication of regular three-dimensional lattices of submicron silicon clusters in an SiO_2 opal matrix, Tech. Phys. Lett. 24 (4) (1998) 326, 327.
[8] V.G. Balakirev, et al., Three-dimensional superlattices in opals, Crystallogr. Rep. 38 (3) (1993) 348–353.
[9] J. Luo, W. Chu, S. Sall, C. Petit, Facile synthesis of monodispersed Au nanoparticles-coated on Stöber silica, Colloids Surf. A Physicochem. Eng. Asp. 425 (2013) 83–91.
[10] X. Yu, Y. Lee, R. Frstenberg, J.O. White, P.V. Braun, Filling fraction dependent properties of inverse opal metallic photonic crystals, Adv. Mater. 19 (2007) 1689–1692.
[11] I. Mitsuteru, H. Uchida, K. Nishimura, P.B. Lim, Magnetophotonic crystals—a novel magneto-optic material with artificial periodic structures, J. Mater. Chem. 16 (2006) 678–684.
[12] M. Inoue, et al., Magnetophotonic crystals, J. Phys. D: Appl. Phys. 39 (2006) R151–R161.
[13] V. Ustinov, A. Rinkevich, D. Perov, M. Samoilovich, S. Klescheva, Anomalous magnetic antiresonance and resonance in ferrite nanoparticles embedded in opal matrix, J. Magn. Magn. Mater. 324 (1) (2012) 78–82.
[14] A.J. Carmona-Carmona, et al., Synthesis and characterization of magnetic opal/Fe_3O_4 colloidal crystall, J. Cryst. Growth 462 (2017) 6–11.
[15] H. Miguez, et al., Control of the photonic crystal properties of the fcc-packed submicrometer SiO_2 spheres by sintering, Adv. Mater. 10 (6) (1998) 480–483.
[16] M. Fang, T.T. Volotinen, S.K. Kulkarni, L. Belova, K.V. Rao, Effect of embedding Fe_3O_4 nanoparticles in silica spheres on the optical transmission properties of three-dimensional magnetic photonic crystals, J. Appl. Phys. 108 (103501) (2010) 1–6.
[17] V. Chabanenko, et al., The magnetic properties of C-Ni carbon-metal complexes, Low Temp. Phys. 43 (5) (2017) 625–630.
[18] H.L. Bhatta, A.E. Aliev, V.P. Drachev, New mechanism of plasmons specific for spin-polarized nanoparticles, Sci. Rep. 9 (2019) 1–8.
[19] W. Stöber, A. Fink, E. Bohn, Controlled growth of monodisperse silica spheres in the micron size range, J. Colloid Interface Sci. 26 (1968) 62–69.
[20] D. Santamaria-Razo, et al., A version of stober synthesis enabling the facile prediction of silica nanospheres size for the fabrication of opal photonic crystals, J. Nanopart. Res. 10 (2008) 1225–1229.
[21] P. Ni, P. Dong, B. Cheng, X. Li, D. Zhang, Synthetic SiO_2 opals, Adv. Mater. 13 (6) (2001) 437–441.
[22] R. Mayoral, et al., 3d long-range orderingrange ordering in an SiO_2 submicrometer-sphere sintered superstructure, Adv. Matter. 9 (3) (1997) 257–260.
[23] A.A. Eliseev, et al., Determination of the real structure of artificial and natural opals on the basis of three dimensional reconstructions of reciprocal space, JETP Lett. 90 (4) (2009) 273–277.
[24] B. Cheng, et al., More direct evidence of the fcc arrangement for artificial opal, Opt. Commun. 170 (1999) 41–46.
[25] L.V. Woodcock, Entropy between the face-centered cubic and hexagonal close-packed crystal structures, Nature 385 (9) (1997) 141–143.
[26] Y. Hou, H. Kondoh, T. Ohta, S. Gao, Size-controlled synthesis of nickel nanoparticles, App. Surf. Sci. 241 (2005) 218–222.
[27] M. Zach, R.M. Penner, Nanocrystalline nickel nanoparticles, Adv. Mater. 12 (12) (2000) 878–883.
[28] S.L. Chen, P. Dong, G.H. Yang, The size dependence of growth rate of monodisperse silica particles from tetraalkoxysilane, J. Colloid Interface Sci. 189 (2) (1997) 268–272.
[29] H. Cong, B. Yu, Fabrication of superparamagnetic macroporous Fe_3O_4 and its derivates using colloidal crystals as templates, J. Colloid Interface Sci. 353 (2011) 131–136.
[30] J.M. Caicedo, et al., Facile route to magnetophotonic crystals by infiltration of 3D inverse opals with magnetic nanoparticles, J. Magn. Magn. Mater. 322 (2010) 1494–1496.
[31] M. Fardis, et al., Structural, static and dynamic magnetic properties of dextran coated γ-Fe_2O_3 nanoparticles studied by ^{57}Fe NMR, Mössbauer, TEM and magnetization measurements, J. Phys. Condens. Matter. 24 (15) (2012) 1–16.
[32] T.J. Bastow, A. Trinchi, NMR analysis of ferromagnets: Fe oxides, Solid State Nucl. Magn. Reson. 35 (2009) 25–31.
[33] V.I. Chizhik, Y.S. Chernyshev, A.V. Donets, V.V. Frolov, A.V. Komolkin, M.G. Shelyapina, Magnetic Resonance and its Applications, Springer, 2014.
[34] M. Wojcik, W. Van Roy, E. Jedryka, S. Nadolski, G. Borghs, J. De Boeck, NMR evidence for MnSb environments within epitaxial NiMnSb films grown on GaAs (001), J. Magn. Magn. Mater. 240 (2002) 414–416.
[35] Y.D. Zhang, W.A. Hines, J.I. Budnick, Z. Zhang, W.M.H. Sachtler, Nuclear magnetic resonance study of the magnetic behavior of ultrafine Co clusters in zeolite NaY, J. Appl. Phys. 76 (1994) 6576–6578.
[36] Y. Liu, J. Luo, Y. Shin, S. Moldovan, O. Ersen, A. Hèbraud, G. Schlatter, C. Pham-Huu, C. Meny, Sampling the structure and chemical order in assemblies of ferromagnetic nanoparticles by nuclear magnetic resonance, Nat. Commun. 7 (2016) 1–7.
[37] T. Kohara, M. Yamaguchi, K. Asayama, NMR study of size effect in ferromagnetic Ni metal, J. Phys. Soc. Jpn. 54 (1985) 1537–1542.
[38] T. J. Bastow, A. Trinchi, NMR analysis of ferromagnets: Fe oxides, Solid State Nucl. Magn. Reson. 35 (25–31).
[39] K.N. Mikhalev, A.Y. Germov, D.A. Prokopyev, M.A. Uimin, A.Y. Yermakov, A.S. Konev, V.S. Gaviko, S.I. Novikov, NMR study of magnetic nanoparticles Ni@C, J. Phys. Conf. Ser. 1389 (012137) (2019) 1–5.
[40] V. Masalov, N.S. Sukhinina, E.A. Kudrenko, G.A. Emelchenko, Mechanism of formation and nanostructure of Stöber silica particles, Nanotechnology 22 (275718) (2011) 1–9.
[41] C.E. Avila-Crisóstomo, E. Sánchez-Mora, V. Garcia-Vazquez, F. Perez-Rodríguez, Magnetic response of Fe nanoparticles embedded in artificial SiO_2 opals, J. Magn. Magn. Mater. 465 (2018) 252–259.
[42] C. Kittel, Introduction to Solid State Physics, 7th ed., John Wiley, New Delhi, 1995.
[43] B. Hallouet, B. Wetzel, R. Pelster, On the dielectric and magnetic properties of nanocomposites, J. Nanomater. 2007 (2007) 1–11.
[44] H.M. Chang, C. Liao, A Parallel Derivation to the Maxwell-Garnett Formula for the Magnetic Permeability of Mixed Materials, WJCMP 1 (2011) 55–58.
[45] A. Bordianu, L. Petrescu, V. Ionita, Numerical testing of homogenization formulas efficiency for magnetic composite materials, J. Phys.: Conf. Ser. 585 (2015) 1–9.
[46] J.D. Jackson, Classical Electrodynamics, John Wiley and Sons, Nueva York, 1962.
[47] L. Landau, E. Lifshitz, On the theory of the dispersion of magnetic permeability in ferromagnetic bodies, Phys. Zeitsch. der Sow. 8 (1935) 153–169.
[48] M.R. Dudek, N. Guskos, B. Grabiec, M. Maryniak, Magnetization dynamics in Landau–Lifshitz–Gilbert formulation. FMR experiment modeling, J. Non-Cryst. Solids 354 (2008) 4146–4150.
[49] S. Jung, J.B. Ketterson, V. Chandrasekhar, Micromagnetic calculations of ferromagnetic resonance in submicron ferromagnetic particles, Phys. Rev. B 66 (132405) (2002) 1–4.
[50] L.F. Shampine, A. Witt, A simple step size selection algorithm for ode codes, J. Comput. Appl. Math. 58 (1995) 345–354.
[51] S.J. Barnett, G.S. Kenny, Gyromagnetic ratios of iron, cobalt, and many binary alloys of iron, cobalt, and nickel, Phys. Rev. 87 (5) (1952) 723–734.